BNL-223518-2022-JAAM

Switching CO2 Electroreduction Selectivity Between C1 and C2 Hydrocarbons on Cu Gas-Diffusion Electrodes

J. Zhang, L. Ma

To be published in "ENERGY & ENVIRONMENTAL MATERIALS"

April 2022

Photon Sciences

Brookhaven National Laboratory

U.S. Department of Energy

USDOE Office of Science (SC), Basic Energy Sciences (BES) (SC-22)

DISCLAIMER

DR. JIANFANG ZHANG (Orcid ID : 0000-0002-3870-4906)
PROF. YUCHENG WU (Orcid ID : 0000-0002-1549-0546)

Article type : Research Article

Article category: (Research Article)
Subcategory: (Electrochemistry)

Switching CO_2 electroreduction selectivity between C_1 and C_2 hydrocarbons on Cu gas diffusion electrodes

Jianfang Zhang[1, 2], Zhengyuan Li[2], Rui Cai[1], Tianyu Zhang[2], Shize Yang[3], Lu Ma[4], Yan Wang[1, *], Yucheng Wu[1, *], Jingjie Wu[2, *]

Dr. J. F. Zhang, R. Cai, Dr. Y. Wang, Prof. Y. C. Wu
School of Materials Science and Engineering, Hefei University of Technology, Hefei 230009, China
E-mail: stone@hfut.edu.cn; ycwu@hfut.edu.cn
Z. Y. Li, T. Y. Zhang, Prof. J. J. Wu
Department of Chemical and Environmental Engineering, University of Cincinnati, Cincinnati, OH 45221, United States
E-mail: jingjie.wu@uc.edu
Dr. S. Z. Yang
Eyring Materials Center, Arizona State University, Tempe, Arizona 85287, United States
Dr. L. Ma
National Synchrotron Light Source II, Brookhaven National Laboratory, Upton, New York, 11971, United States

Keywords: CO_2 electroreduction, electrodeposition, C_2H_4, CH_4, switchable selectivity

Abstract: Regulating the selectivity towards a target hydrocarbon product is still the focus of CO_2 electroreduction. Here we discover that the original surface Cu species in Cu gas diffusion electrodes (GDEs) plays a more important role than the surface roughness, local pH, and facet in governing the selectivity towards C_1 or C_2 hydrocarbons. The selectivity towards C_2H_4 progressively increases while CH_4 decreases steadily upon lowering the Cu oxidation species fraction. At a relatively low electrodeposition voltage of 1.5 V, the Cu GDE with the highest $Cu^{\delta+}/Cu^0$ ratio favors the pathways of *CO hydrogenation to form CH_4 with maximum Faradaic efficiency (FE) of 65.4% and partial current density of 228 mA cm^{-2} at -0.83 V *vs*. RHE. At 2.0 V, the Cu GDE with the lowest $Cu^{\delta+}/Cu^0$ ratio prefers C-C coupling to form C_{2+} products with FE topping 80.1% at -0.75 V *vs*. RHE, where the FE of C_2H_4 accounts for 46.4% and the partial current density of C_2H_4 achieves 279 mA cm^{-2}. This work demonstrates that the selectivity from CH_4 to C_2H_4 is switchable by tuning surface Cu species composition of Cu GDEs.

1. Introduction

Electrocatalytic CO_2 reduction reaction (ECO_2RR) into value-added hydrocarbon fuels and chemicals is a promising technology to recycle carbon, especially when it couples with renewable electricity.[1] Many efforts have been made at the catalyst level to achieve high-performance ECO_2RR in recent years.[2-4] The significant issues of ECO_2RR are still low selectivity towards a single target product, low energy efficiency, and short stability. Copper (Cu) is the only metal that steers ECO_2RR to produce appreciable amounts of hydrocarbons (e.g., CH_4 and C_2H_4) and oxygenates (e.g., C_2H_5OH).[5-7] However, Cu catalysts suffer from high overpotential and low selectivity with wide product distribution from C_1 to C_{2+} products. The key intermediate of adsorbed *CO can be either dimerized at the lower overpotential region or hydrogenated at higher overpotentials, leading to the pathways to the formation of C_2H_4 and CH_4, respectively.[8]

Various studies showed that the activity and selectivity of the C_1-C_2 hydrocarbon products can be tuned by various strategies applied to Cu-based materials surface or interface between the catalyst and electrolyte, such as the control of surface roughness,[9-12] facet,[13, 14] local pH,[15, 16] oxidation state,[17-19] subsurface oxygen,[20] grain boundary,[21-23] and tandem catalysis.[24-27] Morphology-directed ECO_2RR study revealed that the surface roughness of Cu foam catalysts regulates hydrocarbon products. The presence of surface active site and the temporal confining of

gaseous intermediates inside the mesoporous played key role in the selectivity towards C_{2+} products.[11, 28] The variation in morphology of Cu catalysts often triggers the facet-dependent selectivity of ECO_2RR.[14] Extensive theoretical and experimental studies revealed that the Cu (111) facet governs CO_2 reduction pathways for CH_4 generation, while the Cu (100) facet directs the C-C coupling step for C_{2+} products.[13, 29] The bulk electrolyte pH had been demonstrated to have direct influence on the CO_2 reduction performance on Cu catalysts.[16] However, the local pH near the electrode surface often differs from the bulk electrolyte pH due to the dynamic formation of OH^- by coupled H^+/e^- transfer and consumption of OH^- by neutralization with CO_2 in the electrolyte. The difference in roughness results in variation of local pH, which subsequently affects product selectivity on Cu catalysts.[30-32]

Besides, the surface composition of Cu catalyst also plays an essential role in controlling the selectivity and activity toward C_2H_4 or CH_4.[33, 34] However, the authentic active site, namely Cu oxidation species ($Cu^{\delta+}$) versus metallic species (Cu^0), is still under debate.[4, 18, 33, 35] For instance, *in-situ* Raman spectroscopy revealed the surface composition of electrodeposited Cu_2O films was rapidly reduced to metallic Cu^0 during the ECO_2RR.[36] These metallic Cu^0 particles were proposed to be the active catalytic species for CO_2 reduction towards C_2H_4 and C_2H_5OH. The recent study drew the same conclusion that the surface oxide layer on polycrystalline Cu was fully reduced to metallic Cu before the onset potential for CO_2 reduction through *in situ* characterization of grazing incidence X-ray absorption spectroscopy (XAS) and X-ray diffraction (XRD).[37] The findings differed from the previous studies suggesting that Cu^+ species was responsible for C_2H_4 formation.[38] Cu^+ species was resistant to reduction and remained on the surface of oxide-derived copper during the ECO_2RR as illustrated by operando XAS.[38] Additionally, the coexisting of Cu^+ and Cu^0 species on the Cu surface was reported to promote the formation of C_{2+} products synergistically, however, the role of single Cu^+ or Cu^0 species on the adsorption of *CO intermediates remained controversial.[17, 35] The effects of structural morphology, surface oxidation state, local pH, and facet on Cu catalysts are always coupled, which imposes the difficulty to resolve the governing factor that determines the activity and selectivity towards C_1-C_2 hydrocarbons.

Herein, we report that the selectivity of ECO_2RR on Cu gas diffusion electrodes (GDEs) is switchable between C_{2+} products (mainly C_2H_4) and CH_4 by regulating the surface composition of Cu species simply through electrodeposition voltages. The interrogation of physical characterization and electrocatalytic performance shows the governing factor that controls

selectivity towards CO_2 electroreduction is the surface composition of Cu species rather than the surface roughness, local pH, and Cu facet. Low-voltage electrodeposited Cu GDE with a high fraction of $Cu^{\delta+}$ (δ =1 or 2) species prefers producing CH_4 while high-voltage electrodeposited Cu GDE with a low proportion of $Cu^{\delta+}$ species favors C_{2+} products, including predominant C_2H_4. This finding provides insight into the long-standing issue: origin of selectivity diversity in Cu-based catalysts for CO_2 electroreduction.

2. Results and discussion

2.1 Synthesis and characterization of Cu GDEs

The Cu GDEs (Cu-X GDEs, X denotes the deposition voltage) were prepared by the potentiostatic electrodeposition method, as illustrated in Figure 1a. During the synthesis process, Cu foam at the anode was first anodized to form Cu^{2+} ions, while the hydrogen evolution reaction (HER) occurred on the cathode of gas diffusion layer (GDL, Sigracet 35 BC) (Stage I). Most of Cu^{2+} ions were released to the KOH solution, followed by coordination with OH^- ions to form $[Cu(OH)_4]^{2-}$ complexes. The $[Cu(OH)_4]^{2-}$ complexes diffused to the cathode where they were reduced and electrodeposited onto the GDL to form Cu GDEs (Stage II and III). Due to the accumulating formation of $Cu(OH)_2$ on the surface of Cu foam, the predominant reaction on the anode was switched from Cu anodization to oxygen evolution reaction (OER) on $Cu(OH)_2$ (stage III). The corresponding time-dependent current density curves revealed these three stages (Figure 1b). Stage I only lasted for about 35 seconds under the different deposition voltages, indicating the same reactions occurred in stage I. The period of stage II became shorter as the electrodeposition voltage increased. That's because the formation rate of $Cu(OH)_2$ layer was increased by increasing the electrodeposition voltage. At the transition from stage II to stage III, the current density abruptly decreased because the sluggish kinetics OER started to restrict the current density. The electrodeposition on the cathode continued at stage III. However, the electrodeposition rate would decline as the residual $[Cu(OH)_4]^{2-}$ was gradually consumed. We propose the possible reaction mechanism of the electrodeposition process, as demonstrated in the following equations (1-7):

Stage I and II:

Anode $Cu \rightarrow Cu^{2+} + 2e^-$ (stage I and II) (1)

Cathode $2H_2O + 2e^- \rightarrow H_2 + 2OH^-$ (stage I and II) (2)

$$[Cu(OH)_4]^{2-} + 2e^- \rightarrow Cu + 4OH^- \text{ (high voltage, stage II)} \quad (3)$$

and/or $2[Cu(OH)_4]^{2-} + 2e^- \rightarrow Cu_2O + H_2O + 6OH^-$ (low voltage, stage II) (4)

Stage III:

Anode $4OH^- \rightarrow O_2 + 2H_2O + 4e^-$ (5)

Cathode $[Cu(OH)_4]^{2-} + 2e^- \rightarrow Cu + 4OH^-$ (high voltage) (6)

and/or $2[Cu(OH)_4]^{2-} + 2e^- \rightarrow Cu_2O + H_2O + 6OH^-$ (low voltage) (7)

The real-time electrodeposition process at 1.5 V was captured by the photo images (Figure S1). The color of Cu foam changed from brick-red to dark green as the electrodeposition proceeded (Figure S2), illustrating that the generated Cu^{2+} ions nearby the Cu foam were turned into $Cu(OH)_2$ which was coated onto the surface of Cu foam. We observed hydrogen gas bubbles resulting from HER on the cathode while no oxygen gas bubbles emerged on the anode in the stage I and II of the electrodeposition process (Figure S2). However, after the formation of a thick $Cu(OH)_2$ layer on the Cu foam as the electrodeposition elapsed beyond 900 seconds, a significant number of oxygen gas bubbles appeared due to OER on the anode. These results support the proposed three-stage mechanism of the electrodeposition process.

The electrodeposition voltage plays a significant role in regulating the morphology and bulk composition of the as-prepared Cu GDEs. The scan electron microscopy (SEM) images show that Cu GDEs possess distinct morphologies by varying the electrodeposition voltage (Figure 1c and S3). Of note, the different electrodeposition voltage would cause the different electrodeposition time between stage II and III, especially for the stage II. The hydrogen bubbules generated in stage II from the hydrogen evolution reaction would affect the morphology structure and size of the as-prepared Cu GDEs. The Cu-1.5 GDE exhibited a nano-mulberry structure composed of some small tetrahedron nanoparticles. When increasing the voltage to 1.6 V, tetrahedron nanoparticles were also presented in nano-mulberry structure, but the size of the nano-mulberry became larger due to the decreasing amount of the released hydrogen bubbules on the cathode. The size of the nano-mulberry increased continuously as the voltage increased up to 1.8 V. However, the morphology of nanoparticles in nano-mulberry changed from tetrahedrons to cubes as the voltage increased to 1.7 V, and evolved into irregular spheres when the voltage rose to 1.8 V. When the voltage exceeded 1.8 V, the morphology of the Cu nanoparticles became quasi-polyhedral

structure with a decreased size. The TEM images show a tetrahedron shape of the Cu-1.5 GDE (Figure 2a), a cube shape of Cu-1.7 (Figure 2b), and a quasi-polyhedral structure of Cu-2.0 (Figure 2c), which are consistent with the SEM results. The HRTEM image, combined with the corresponding fast Fourier transform (FFT) diffraction pattern in Figures 2d, reveals the Cu_2O (111) plane with the lattice distance of 0.243 nm in Cu-1.5, and Figures 2e and f show the Cu (200) and Cu (111) planes with the lattice distance of 0.181 and 0.208 nm in Cu-1.7 and Cu-2.0, respectively.

The XRD results show that all the Cu GDEs present a dominant phase of metallic Cu^0 with the diffraction peaks at $2\theta = 43.3°$, 50.4°, and 74.1° corresponding to (111), (200), and (220) plane, respectively (Figure 2g). The diffraction peaks of Cu_2O phase are discernable for Cu-1.5 and Cu-1.6, indicating the coexisting of Cu and Cu_2O phases in the Cu GDEs prepared by low electrodeposition voltages. The intensities are weakened with the increase in electrodeposition voltage, and Cu_2O diffraction peaks even disappear at high electrodeposition voltages of 1.9 and 2.0 V. To further obtain structural information of Cu GDEs, the XAS was performed for Cu-1.5 and Cu-2.0 GDEs. The Cu K-edge XANES of Cu-1.5 and Cu-2.0 agree well with that for the Cu foil (Figure 2h). The corresponding EXAFS results show that the Cu-1.5 and Cu-2.0 GDEs have the same coordination structure as the Cu foil (Figure 2i). Thus, the XAS results confirm that metallic Cu^0 prevails in both Cu-1.5 and Cu-2.0 GDEs.

The electrodeposition voltage gradually regulates the Cu surface composition of the as-prepared Cu GDEs as well. The peaks of X-ray photoelectron spectroscopy (XPS) spectra for Cu $2p_{3/2}$ and Cu $2p_{1/2}$ can be deconvoluted into two subpeaks: a dominant subpeak at lower binding energy for Cu^0/Cu^+ and a secondary subpeak at higher binding energy for Cu^{2+} (Figure 3a). The formation of minor Cu^{2+} species is attributed to the oxidation of Cu^0/Cu^+ species, especially Cu^+, in the alkaline solution. The ratio of $Cu^{2+}/(Cu^+ + Cu^0)$ (or the percent of Cu^{2+} species) progressively declines with the increase of the electrodeposition voltage. For example, the $Cu^{2+}/(Cu^+ + Cu^0)$ ratio decreases from 1.49 for Cu-1.5 GDE to 0.66 for Cu-2.0 GDE (Figure 3a and Table S1). The Cu LMM spectra distinguish Cu^+ (kinetic energy of 916.4 eV) from Cu^0 (kinetic energy of 918.2 eV) as shown in Figure 3b. The Cu LMM spectra show that the ratio of Cu^+/Cu^0 (or the fraction of Cu^+) also decreases with the increase of electrodeposition voltage (Table S1 and S2), corroborating the XRD results. Note that the ratio of Cu^{2+}/Cu^+ also decreases as the electrodeposition voltage rises, as derived from Cu 2p and Cu LMM spectra and confirmed by O

1s spectroscopy (Figure 3c and Table S1). Specifically, the content of Cu^{2+} is almost two-fold of Cu^{+} for Cu-1.5 GDE and decreases to 1.33 times for Cu-2.0 GDE.

3.2 Electrocatalytic performance for CO_2 reduction

The electrochemical performance of the Cu GDEs for electrocatalytic CO_2 reduction reaction (ECO_2RR) was evaluated in a flow cell (Figure S4) operated under the potentiostatic mode. The selectivity towards C_1 hydrocarbon and C_{2+} products, including C_2H_4 and C_2H_5OH, is switchable on electrodeposited Cu GDEs (Figure 4 and Figure S5-6). Interestingly, the Cu-1.5 GDE achieved the highest selectivity of CH_4 production among all GDEs, with the FE of CH_4 reaching 65.4% at a cathodic potential of -0.83 V (Figure 4a). In contrast, the FE of C_2H_4 was less than 3.5% at the same potential (Figure 4c). However, the selectivity was gradually shifted from CH_4 to C_{2+} products as the electrodeposition voltage increased from 1.5 to 1.9 V. The FE for C_{2+} products achieved a maximum of 82.2% for the Cu-1.9 GDE at -0.73 V. Further increasing the electrodeposition voltage to 2.0 V, the top FE of total C_{2+} products slightly declined to 80.1% as well as that of C_2H_5OH decreased from 32.0% to 26.3% at -0.75 V (Figure 4e and S5d). However, the FE of C_2H_4 kept increasing, which reached a maximum of 46.4% at -0.75 V (Figure 4c). Meanwhile, the CH_4 selectivity was suppressed to 1.6% at -0.75 V for the Cu-2.0 GDE (Figure 4a). Accompanied with the shift of selectivity to C_{2+} products, the total current densities of ECO_2RR for Cu GDEs monotonically increased as the electrodeposition voltage increased, surging from 350 mA cm^{-2} for the Cu-1.5 GDE to 750 mA cm^{-2} for the Cu-2.0 GDE at around -0.83 V (Figure S7). Corresponding to the selectivity shift, the partial current density of CH_4 (j_{CH_4}) decreased from Cu-1.5 to Cu-2.0 GDEs, whereas both partial current densities of C_2H_4 ($j_{C_2H_4}$) and C_{2+} products ($j_{C_{2+}}$) increased (Figure 4b, d, and f). The Cu-1.5 GDE exhibited j_{CH_4} as high as 228 mA cm^{-2} and $j_{C_{2+}}$ as low as 11 mA cm^{-2} at around -0.83 V. In comparison, the Cu-2.0 GDE achieved the maximum $j_{C_2H_4}$ of 279 mA cm^{-2} and $j_{C_{2+}}$ of 482 mA cm^{-2} at the identical potential.

3.3 Identification of the origin of catalytic selectivity and activity

The switchable electrocatalytic activity and selectivity towards CO_2 electroreduction on these electrodeposited Cu GDEs are hypothesized to be resulted from the change of morphology and surface Cu species composition at different electrodeposition voltages. The effect of surface roughness or electrochemical active surface area (ECSA) in Cu GEDs with different morphologies was studied first. The ECSA, which reflects the number of accessible active sites in the Cu GDEs, can be estimated by measuring the double-layer capacitance (C_{dl}) of the electrode-electrolyte

interface via the cyclic voltammetry method (Figure S8-S9 and Table S3). In general, the ECSA-normalized $j_{C_2H_4}$ increases while ECSA-normalized j_{CH_4} decreases as the ECSA rises from Cu-1.5 GDE to Cu-2.0 GDE. However, the ratio of ECSA-normalized $j_{C_2H_4}$ of Cu-2.0 GDE to Cu-1.5 GDE is only 7.9 at -0.83 V, which is much lower than that of geometric $j_{C_2H_4}$(23.9) (Figure S10). Conversely, the ratio of ECSA-normalized j_{CH_4} (13.5) of Cu-1.5 GDE to Cu-2.0 GDE is higher than that of geometric j_{CH_4} (5.8) at -0.83 V (Figure S10). These results demonstrate that the surface roughness itself cannot fully account for the switchable activity and selectivity towards CO_2 electroreduction on these different Cu GEDs.

Next, we focused on the effect of surface roughness induced difference in local pH on the selectivity towards CH_4 and C_{2+} products. The ECO_2RR performance over Cu-1.5, Cu-1.7, and Cu-2.0 GDEs was first investigated and compared in electrolytes with different bulk pH values, including 1 M $KHCO_3$, 1 M KOH, and 5 M KOH. For these three GDEs, the FE_{CH_4} slightly decreased with the increasing of bulk electrolyte pH while a reverse trend was observed for $FE_{C_{2+}}$ (Figure S11). Take Cu-1.5 GDEs as an example, the FE_{CH_4} decreased 14% by changing the electrolyte from 1 M $KHCO_3$ to 5 M KOH while the corresponding $FE_{C_{2+}}$ increased 24%. The results indicate that the low pH favors the ECO_2RR towards CH_4 while high pH promotes the formation of C_{2+} products, consistent with the previously reported works.[31, 32] However, there were no significant changes in selectivity of both CH_4 and C_{2+} products among these three GDEs at the same electrolyte of either 1 M $KHCO_3$ or 5 M KOH, suggesting that the bulk electrolyte pH has little influence on the reaction pathways between CH_4 and C_{2+} products on the same GDE. The local pH near the Cu GDE surface differentiates from that in the bulk electrolyte due to the CO_2-OH^- neutralization reaction. The peak area ratio of CO_3^{2-}/HCO_3^- can be used to estimate the local pH based on the Henderson-Hasselbach equation: pH = pK_a + log(CO_3^{2-}/HCO_3^-), where K_a is acid dissociation constant.[15] The local pH nearby the surface of GDEs can be calculated from the calibration curve by measuring in-situ Raman spectra (Figure S12-S13).[39] The local pH of all three GDEs slightly increased as the cathode potential was negatively swept (Figure S14), indicating the formation rate of OH^- in CO_2 reduction process was faster than its consumption rate by the neutralization reaction. Interestingly, these three GDEs displayed almost equivalent local pH values at each potential, indicating the similar local reaction environment during the ECO_2RR. Taken the results of bulk pH effect and local pH measurement together, we conclude that the local pH variation is not the main factor that controls the selectivity between CH_4 and C_{2+} products.

Afterwards, we investigated the influence of Cu facet on the activity and selectivity towards CO_2 electroreduction. The morphologies of Cu GDEs were well-maintained after ECO_2RR, as shown in the SEM images (Figure S15). The HRTEM images reveal the distinguished lattice plane of Cu (111), Cu (200), and Cu (111) facets with distances of 0.208, 0.181, and 0.208 nm for Cu-1.5, Cu-1.7, and Cu-2.0, respectively (Figure S16). Of note, most of the oxide layer on Cu-1.5 was reduced to metallic Cu after ECO_2RR, as evidenced by XRD and XAS results (Figure S17 and S18). The Cu-1.5 GDE with dominant exposed Cu (111) facet exhibited the main CH_4 product. When Cu (200) facet was primarily exposed on Cu-1.7 GDE, the production rate and selectivity of C_2H_4 increased, accompanied by the decrease of CH_4 product. However, the Cu-2.0 GDE with prevailing Cu (111) facet exhibited the highest selectivity towards C_2H_4 and C_{2+} products, indicating facet alone cannot be accountable for the difference in activity and selectivity.

Finally, the dependence of the reactivity towards CO_2 electroreduction on the surface composition was studied. The ratio of $Cu^{\delta+}/Cu^0$ ($Cu^{\delta+} = Cu^{2+} + Cu^+$) declined from 12.32 for Cu-1.5 to 2.30 for Cu-2.0 (Table S1). The ratios of Cu^+/Cu^0 and Cu^{2+}/Cu^+ followed the same tendency. The Cu-1.5 GDE surface, preferring CH_4 formation, was primarily constituted of Cu^{2+}+Cu^+ species with a total percentage of 92.5% (Table S2). By contrast, Cu-2.0 GDE, achieving the highest production rate of C_2H_4, had 70.0% $Cu^{\delta+}$ species and 30.0% Cu^0. This distinguishable result referred to the most important role of surface Cu species in selectivity towards ECO_2RR. Of note, the ratio of $Cu^{\delta+}/Cu^0$ in Cu GDEs decreased after ECO_2RR (Figure S19 and Table S4-S5), indicating that the $Cu^{\delta+}$ species can be reduced to Cu^0 species during ECO_2RR, which was consistent with our XRD and XAS results as well as previous results from operando analysis.[27] However, the content of Cu^+ and Cu^{2+}species in the Cu GDEs still followed the order of Cu-1.5 > Cu-1.7 > Cu-2.0 after ECO_2RR. The surface Cu species composition under ECO_2RR process cannot be accurately reflected by XPS due to the possible re-oxidation of Cu exposed in the air, which requires more advanced analysis techniques in the future work. Nevertheless, our result shows that both $FE_{C_2H_4}/FE_{CH_4}$ and $FE_{C_{2+}}/FE_{CH_4}$ ratios are inversely proportional to $Cu^{\delta+}/Cu^0$ ratio for the pristine Cu samples (Figure 5a and b). The Cu-2.0 GDE with the lowest $Cu^{\delta+}/Cu^0$ ratio (Cu^+/Cu^0 ratio of 0.99) achieved the highest $FE_{C_2H_4}/FE_{CH_4}$ and $FE_{C_{2+}}/FE_{CH_4}$ ratios among the six GDEs. The maximum $FE_{C_2H_4}/FE_{CH_4}$ and $FE_{C_{2+}}/FE_{CH_4}$ reached 48.6 and 89.5, respectively, for Cu-2.0 GDE at -0.66 V. These results suggest that the high $Cu^{\delta+}/Cu^0$ ratio (Cu^+/Cu^0 ratio of 2.54) on the Cu surface favors the C_1 hydrocarbon formation, while the low $Cu^{\delta+}/Cu^0$ ratio (Cu^+/Cu^0 ratio of

0.99) facilitates the C-C coupling for C_{2+} products. This trend is consistent with the prior findings that demonstrated the oxide-derived Cu surface composed of Cu^0 and Cu^+ with equal amount enhances the selectivity towards C_{2+} products.[40] Combined all above results, we may safely reach a conclusion that the selectivity towards CO_2 reduction is principally governed by the $Cu^{\delta+}/Cu^0$ ratio over the surface roughness, local pH, and facet in different Cu GDEs.

3.4 Mechanism of CO_2 reduction reaction

Several previous studies proposed that *CO is the key intermediate for CO_2 conversion.[21, 41-43] CH_4 pathway is proceeded by hydrogenation of *CO to *CHO intermediate while the pathway towards C_{2+} products mainly lies in CO dimerization (C-C coupling) step especially at the low overpotential region.[21, 44] We posited that such different selectivity of CH_4 and C_{2+} products on our Cu GDEs is attributed to the difference in *CO surface coverage. We analyzed the CO generation rate and dimerization rate over six Cu GDEs aforementioned to unravel the underlying reaction mechanism towards CO_2 conversion. The CO generation rate is the sum of the production rates of C_{2+}, CH_4, and CO products normalized by the electrons transferred per mole of product assuming CO is the reactant. The CO dimerization rate is referred to normalized production rates of C_{2+} products (See detailed calculation in SI). The CO generation rate increases in the order from Cu-1.5 to Cu-2.0 GDEs (Figure 5c), indicating that the coverage of *CO on the electrode is greatly enhanced from Cu-1.5 to Cu-2.0 GDEs, especially at more negative potentials (< -0.75 V). Generally, the high *CO surface coverage promotes the C-C coupling reaction kinetics on the Cu surface, while the low *CO surface coverage favors the hydrogenation of *CO to *CHO, the critical step to CH_4 formation.[16, 45-47] Accordingly, an analogous increasing trend of CO dimerization rate can be observed from Cu-1.5 to Cu-2.0 GDEs (Figure 5d). These results validate that the Cu-2.0 GDE generates sufficient CO to increase the *CO surface coverage, leading to the acceleration of CO-to-C_{2+} products conversion. To further study the reaction kinetics in terms of CO intermediate reactant, the Tafel plots of CO generation and dimerization were analyzed (Figure 5e and f). The Cu-2.0 GDE displays the smallest Tafel slopes of both CO generation and CO dimerization reactions, illustrating the fastest production rate of C_{2+} products.

In-situ Raman spectroscopy was performed in a flow cell to further investigate the adsorption property of reaction intermediates during ECO_2RR (Figure 6a-c). Two weak Raman signals of * $CO_2^{\cdot-}$ at 735 and 1556 cm^{-1} could be observed in Cu-1.5 GDE at potentials larger than -0.3 V and then the signals disappeared at more negative potentials. The Raman signals of *$CO_2^{\cdot-}$ peaks increased for Cu-1.7 GDE and was further enhanced for Cu-2.0 GDE. The higher intensity of *

$CO_2^{\cdot-}$ peaks reflected a strong adsorption of $*CO_2^{\cdot-}$ intermediate on the surface of Cu-2.0 GDE, indicating more stabilized $*CO_2^{\cdot-}$ intermediate on Cu-2.0 GDE. The $*CO_2^{\cdot-}$ radical anion is regarded as the first reaction intermediate for ECO_2RR, which can be further reduced to form the second key intermediate of *CO for hydrocarbons.[48] Therefore, the strong adsorption/stabilization of $*CO_2^{\cdot-}$ intermediate promotes the conversion of CO_2 to *CO intermediate.[48, 49] A similar peak intensity tendency of *CO intermediate adsorption behavior could be revealed among Cu-1.5, Cu-1.7, and Cu-2.0 GDEs. The Cu-2.0 GDE showed the strongest Raman peaks corresponding to *CO at 301, 398, and 2060 cm^{-1}, which are assigned to the Cu-CO frustrated rotation, Cu-CO stretch, and C≡O stretch, respectively.[50, 51] This result demonstrates that the Cu-2.0 GDE provides abundant active sites for efficient conversion of $*CO_2^{\cdot-}$ to *CO intermediate, leading to high *CO surface coverage on Cu-2.0 GDE, which agrees well with the calculation results of CO generation rate above.

Previous studies implied that the surface components of $Cu^{\delta+}$ and Cu^0 in Cu-based catalysts governed product selectivity by tailoring the adsorption of *CO intermediates.[52, 53] Our in-situ Raman results also suggest that $Cu^{\delta+}/Cu^0$ ratio might play an essential role in tuning *CO adsorption. As shown in Figure 6a-c, the peak at 536 cm^{-1} appears, which is assigned to the $CuO_x/(OH)_y$ species.[54] Cu-1.5 and Cu-1.7 GDEs displayed high peak intensity of $CuO_x/(OH)_y$ while Cu-2.0 GDE showed a relatively low peak intensity, suggesting the higher content of $Cu^{\delta+}$ species can be remained in Cu-1.5 and Cu-1.7 GDEs. Moreover, to probe the stability of the surface $Cu^{\delta+}$ species in the Cu GDEs during CO_2 reduction, we further investigate the in-situ Raman spectra of Cu-1.5 and Cu-2.0 GDEs under continuous CO_2 reduction at -0.45 V for 140 min, as shown in Figure S20. Both Cu-1.5 and Cu-2.0 GDEs exhibit a peak of $CuO_x/(OH)_y$ species in the long-term test, demonstrating the stability of surface $Cu^{\delta+}$ species during CO_2 reduction. Although the in-situ Raman test cannot precisely quantify the amount of $Cu^{\delta+}$ species in the Cu GDEs, it can be well reflected the dynamic change of Cu species during CO_2 reduction. The possible reaction mechanism of the formation of CH_4 and C_2H_4 on Cu surfaces was proposed and depicted in Figure 6d. In the case of Cu-1.5 GDE with dominant Cu^+, the low *CO surface coverage results in a high energy barrier for C-C coupling that suppresses C_{2+} generation while leading to hydrogenation step for CH_4 production. When the Cu^0 species fraction increases in the Cu GDE as the electrodeposition voltage increases, more *CO intermediate emerges on the Cu surface, especially at more negative overpotentials. The nearly equal content of Cu^+ and Cu^0 in

Cu-2.0 GDE will generate abundant amount of *CO intermediate, providing high *CO surface coverage, which assists in dimerizing CO to form C_{2+} products.[17, 35]

3. Conclusion

In summary, we regulated the morphology and surface Cu species composition of Cu GDEs by simply changing the electrodeposition voltage. The selectivity of CO_2 electroreduction is switched from CH_4 to C_{2+} products upon lowering the fraction of Cu oxidation species. The Cu-1.5 GDE with the highest $Cu^{\delta+}/Cu^0$ ratio favors *CO hydrogenation pathways to form CH_4. When lowering the $Cu^{\delta+}/Cu^0$ ratio to the medium value, the Cu-1.7 GDE generates both C_2H_4 and CH_4 in an appreciable selectivity. In contrast, the Cu-2.0 GDE with the lowest $Cu^{\delta+}/Cu^0$ ratio prefers *CO dimerization to form C_{2+} products. The highest FE of CH_4 for Cu-1.5 GDE reaches 65.4% at -0.83 V, at which the partial current density achieves 228 mA cm^{-2}. Compared to Cu-1.5, the FE of CH_4 for the Cu-2.0 GDE is minimized to 1.6% at -0.75 V, while the FE of C_2H_4 tops 46.4% with a partial current density of 279 mA cm^{-2} at this potential. This work reveals the strong dependence of reactivity towards CO_2 reduction on original surface Cu species composition rather than surface roughness, local pH, and Cu facet. Future work should focus on the unravelling of the underlying effect of Cu species evolution during the reaction process on the switchable selectivity from CH_4 to C_2H_4.

4. Experimental section

4.1. Synthesis of samples

The Cu GDEs were prepared by the potentiostatic electrodeposition. In a two-electrode cell, pure Cu foam and GDL with each size of 2 × 2 cm^2 were worked as anode and cathode, respectively. The GDL (purchased from SGL Sigracet 35 BC) was composed of microporous carbon layer with 5% PTFE treatment and carbon fiber paper support. The distance between the anode and cathode was set to 2 cm. The aqueous solution of 3.0 M KOH was used as th e electrolyte. The electrodeposition was carried on a Gamry electrochemical workstation (Gamry Interface 1010E) using a chronoamperometry mode with a duration of 0.5 h. The electrodeposition time of 0.5 h is chosed based on the theoretical calculation of the charges obtained from the time-dependent current density curves (See detailed calculation in SI). Six Cu GDEs were synthesized

with different electrodeposition voltages of 1.5, 1.6, 1.7, 1.8, 1.9, and 2.0 V, which are denoted as Cu-1.5, Cu-1.6, Cu-1.7, Cu-1.8, Cu-1.9, and Cu-2.0, respectively.

4.2 Materials characterization

T The morphology of the as-prepared Cu GDEs was imaged by a SU8020 field emission scan electron microscopy (FESEM). The crystalline structure was identified by XRD (Rigaku D/MAX2500VL). The lattice structure was analyzed by a JEM-2100F field emission transmission electron microscope (TEM). The Cu samples' surface chemical composition was determined by X-ray photoelectron spectroscopy (XPS, ESCALAB250Xi). The bulk composition was measured by XAS at National Synchrotron Light Source II at Brookhaven National Laboratory.

4.3 Electrochemical measurement

The electrochemical measurements were performed on a Gamry electrochemical workstation. A flow cell equipped with cathodic and anodic compartments separated by an anion exchange membrane (Fumasep FAA-3-PK-75) was used as a reactor. The as-prepared Cu GDEs were directly used as a cathode with an active reaction area of 1×1 cm^2. A Ni foam of an area 2×2 cm^2 pressed onto a GDL was used as an anode. The electrolyte of 1.0 M KOH was pumped to the two compartments with a flow rate of 0.5 ml min^{-1}. High-purity CO_2 gas was purged into the cathode with a flow rate of 15.0 sccm. A constant cell voltage was applied to the flow cell during CO_2 electrolysis. A Ag/AgCl (saturated KCl) electrode was linked to the cathode to measure the electrode potential. The solution resistance (R_s) was determined by potentiostatic electrochemical impedance spectroscopy (EIS) measurement under an open circuit potential at frequencies ranging from 0.1 Hz to 100 kHz. All potentials were converted to a reversible hydrogen electrode (RHE) scale with manual iR_s compensation: $E_{RHE} = E_{Ag/AgCl} + 0.059 \times pH + 0.197 - iR_s$. Before the electrocatalytic test, the cathode was pretreated by cyclic voltammetry from -0.5 to -1.0 V vs. RHE for 3 cycles. The double-layer capacitance of each electrode was estimated from the cyclic voltammetric curves with different scan rates. The electrochemical active surface area (ECSA) of the electrodes was calculated based on the double-layer capacitance of each electrode.

4.4 Products determination

The gaseous products, including H_2, CO, CH_4, and C_2H_4 were detected by on-line gas chromatography (GC 5890, Agilent) equipped with a thermal conductivity detector (TCD) and a flame ionization detector (FID). High purity helium (He) gases were used as the carrier gas. The outlet gas stream was injected into GC after an electrocatalytic test for 3 min at each potential. The

liquid products were quantified by ^{1}H NMR (Bruker AV 400 MHz spectrometer). To prepare the NMR samples, 500 µl of the collected electrolyte was mixed with 100 µl D_2O solution consisting of 5 mM of 3-(trimethylsilyl)propionic-2,2,3,3-d_4 acid sodium salt (TSP).

Supporting Information

Supporting Information is available from the Wiley Online Library or from the author.

Notes

The authors declare no competing financial interest.

Acknowledgements

This work was partially financially supported by NSF CBET-2033343. J. Z. thanks the support from National Natural Science Foundation of China (52172293, 51772072 and 51672065) and the Fundamental Research Funds for the Central Universities (JZ2021HGQB0282 and PA2021GDSK0088). Y. W. and Y. W. also would like to acknowledge the financial support from the Key R&D Projects of Anhui Province (202104b11020016) and the 111 Project (B18018). This research used resources of the National Synchrotron Light Source II, a U.S. Department of Energy (DOE) Office of Science User Facility operated for the DOE Office of Science by Brookhaven National Laboratory under Contract No. DE-SC0012704. We acknowledge the use of facilities within the Eyring Materials Center at Arizona State University supported in part by NNCI-ECCS-1542160.

Received: (will be filled in by the editorial staff)
Revised: (will be filled in by the editorial staff)
Published online: (will be filled in by the editorial staff)

References

[1] Y. Y. Birdja, E. Pérez-Gallent, M. C. Figueiredo, A. J. Göttle, F. Calle-Vallejo, M. T. M. Koper, *Nat. Energy* **2019**, *4*, 732-745.

[2] A. S. Varela, W. Ju, T. Reier, P. Strasser, *ACS Catal.* **2016**, *6*, 2136-2144.

[3] M. Ma, K. Djanashvili, W. A. Smith, *Angew. Chem. Int. Ed.* **2016**, 55, 6680-6684.

[4] Y. Kim, S. Park, S.-J. Shin, W. Choi, B. K. Min, H. Kim, W. Kim, Y. J. Hwang, *Energy Environ. Sci.* **2020**, 13, 4301-4311.

[5] L. Wang, S. Nitopi, A. B. Wong, J. L. Snider, A. C. Nielander, C. G. Morales-Guio, M. Orazov, D. C. Higgins, C. Hahn, T. F. Jaramillo, *Nat. Catal.* **2019**, *2*, 702-708.

[6] R. M. Arán-Ais, F. Scholten, S. Kunze, R. Rizo, B. R. Cuenya, *Nat. Energy.* **2020**, *5*, 317-325.

[7] M. Zhong, K. Tran, Y. Min, C. Wang, Z. Wang, C. T. Dinh, P. De Luna, Z. Yu, A. S. Rasouli, P. Brodersen, S. Sun, O. Voznyy, C. S. Tan, M. Askerka, F. Che, M. Liu, A. Seifitokaldani, Y. Pang, S. C. Lo, A. Ip, Z. Ulissi, E. H. Sargent, *Nature* **2020**, *581*, 178-183.

[8] A. A. Peterson, F. Abild-Pedersen, F. Studt, J. Rossmeisl, J. K. Nørskov, *Energy Environ. Sci.* **2010**, *3*, 1311-1315.

[9] A. Loiudice, P. Lobaccaro, E. A. Kamali, T. Thao, B. H. Huang, J. W. Ager, R. Buonsanti, *Angew. Chem. Int. Ed.* **2016**, *55*, 5789-5792.

[10] T. T. H. Hoang, S. Verma, S. Ma, T. T. Fister, J. Timoshenko, A. I. Frenkel, P. J. A. Kenis, A. A. Gewirth, *J. Am. Chem. Soc*. **2018**, *140*, 5791-5797.

[11] K. D. Yang, W. R. Ko, J. H. Lee, S. J. Kim, H. Lee, M. H. Lee, K. T. Nam, *Angew. Chem. Int. Ed.* **2017**, *56*, 796-800.

[12] A. Dutta, M. Rahaman, N. C. Luedi, M. Mohos, P. Broekmann, *ACS Catal.* **2016**, *6*, 3804-3814.

[13] W. Luo, X. Nie, M. J. Janik, A. Asthagiri, *ACS Catal.* **2015**, *6*, 219-229.

[14] P. Iyengar, J. Huang, G. L. De Gregorio, C. Gadiyar, R. Buonsanti, *Chem. Commun.* **2019**, 55, 8796-8799.

[15] D. A. Henckel, M. J. Counihan, H. E. Holmes, X. Chen, U. O. Nwabara, S. Verma, J. Rodríguez-López, P. J. A. Kenis, A. A. Gewirth, *ACS Catal.* **2020**, *11*, 255-263.

[16] X. Liu, P. Schlexer, J. Xiao, Y. Ji, L. Wang, R. B. Sandberg, M. Tang, K. S. Brown, H. Peng, S. Ringe, C. Hahn, T. F. Jaramillo, J. K. Norskov, K. Chan, *Nat. Commun.* **2019**, *10*, 32.

[17] T. C. Chou, C. C. Chang, H. L. Yu, W. Y. Yu, C. L. Dong, J. J. Velasco-Velez, C. H. Chuang, L. C. Chen, J. F. Lee, J. M. Chen, H. L. Wu, *J. Am. Chem. Soc*. **2020**, *142*, 2857-2867.

[18] S. Y. Lee, H. Jung, N. K. Kim, H. S. Oh, B. K. Min, Y. J. Hwang, *J. Am. Chem. Soc*. **2018**,

140, 8681-8689.

[19] A. A. Permyakova, J. Herranz, M. El Kazzi, J. S. Diercks, M. Povia, L. R. Mangani, M. Horisberger, A. Patru, T. J. Schmidt, *Chemphyschem* **2019**, *20*, 3120-3127.

[20] M. Favaro, H. Xiao, T. Cheng, W. A. Goddard III, J. Yano, E. J. Crumlinb, *Proc. Natl. Acad. Sci. U. S. A.*, **2017**, *114* (26) 6706-6711.

[21] C. Tang, J. Shi, X. Bai, A. Hu, N. Xuan, Y. Yue, T. Ye, B. Liu, P. Li, P. Zhuang, J. Shen, Y. Liu, Z. Sun, *ACS Catal.* **2020**, *10*, 2026-2032.

[22] R. G. Mariano, K. McKelvey, H. S. White, M. W. Kanan, *Science* **2017**, *358*, 1187-1192.

[23] X. Feng, K. Jiang, S. Fan, M. W. Kanan, *J. Am. Chem. Soc*. **2015**, *137*, 4606-4609.

[24] C. G. Morales-Guio, E. R. Cave, S. A. Nitopi, J. T. Feaster, L. Wang, K. P. Kuhl, A. Jackson, N. C. Johnson, D. N. Abram, T. Hatsukade, C. Hahn, T. F. Jaramillo, *Nat. Catal*. **2018**, *1*, 764-771.

[25] X. She, T. Zhang, Z. Li, H. Li, H. Xu, J. Wu, *Cell Rep. Phys. Sci*. **2020**, *1*, 100051.

[26] T. Zhang, Z. Li, J. Zhang, J. Wu, *J. Catal*. **2020**, *387*, 163-169.

[27] S. Zhang, S. Zhao, D. Qu, X. Liu, Y. Wu, Y. Chen, W. Huang, *Small* **2021**, e2102293.

[28] D. Raciti, K. J. Livi, C. Wang, *Nano Lett*, 2015, 15, 6829-6835.

[29] G. Mangione, J. Huang, R. Buonsanti, C. Corminboeuf, *J. Phys. Chem. Lett*. **2019**, *10*, 4259-4265.

[30] N. Gupta, M. Gattrell, B. MacDougall, *J. Appl. Electrochem.* **2005**, 36, 161-172.

[31] R. Kas, R. Kortlever, H. Yılmaz, M. T. M. Koper, G. Mul, *ChemElectroChem* **2015**, *2*, 354-358.

[32] A. S. Varela, M. Kroschel, T. Reier, P. Strasser, *Catal. Today* **2016**, *260*, 8-13.

[33] F. Dattila, R. García-Muelas, N. López, *ACS Energy Lett.* **2020**, *5*, 3176-3184.

[34] R. Kas, R. Kortlever, A. Milbrat, M. T. Koper, G. Mul, J. Baltrusaitis, *Phys. Chem. Chem. Phys*. **2014**, *16*, 12194-12201.

[35] H. Bai, T. Cheng, S. Li, Z. Zhou, H. Yang, J. Li, M. Xie, J. Ye, Y. Ji, Y. Li, Z. Zhou, S. Sun, B. Zhang, H. Peng, *Sci. Bull.* **2021**, *66*, 62-68.

[36] D. Ren, Y. L. Deng, A. D. Handoko, C. S. Chen, S. Malkhandi, B. S. Yeo, *ACS Catal.* **2015**, *5* (5), 2814-2821.

[37] S. H. Lee, J. C. Lin, M. Farmand, A. T. Landers, J. T. Feaster, J. E. Aviles Acosta, J. W. Beeman, Y. Ye, J. Yano, A. Mehta, R. C. Davis, T. F. Jaramillo, C. Hahn, W. S. Drisdell, *J. Am. Chem. Soc*. **2021**, *143*, 588-592.

[38] H. Mistry, A. S. Varela, C. S. Bonifacio, I. Zegkinoglou, I. Sinev, Y. W. Choi, K. Kisslinger, E. A. Stach, J. C. Yang, P. Strasser, B. R. Cuenya, *Nat. Commun.* **2016**, *7*, 12123.

[39] X. Chen, J. Chen, N. M. Alghoraibi, D. A. Henckel, R. Zhang, U. O. Nwabara, K. E. Madsen, P. J. A. Kenis, S. C. Zimmerman, A. A. Gewirth, *Nat. Catal.* **2020**, *4*, 20-27.

[40] S. C. Lin, C. C. Chang, S. Y. Chiu, H. T. Pai, T. Y. Liao, C. S. Hsu, W. H. Chiang, M. K. Tsai, H. M. Chen, *Nat. Commun*. **2020**, *11*, 3525.

[41] M. Dunwell, W. Luc, Y. Yan, F. Jiao and B. Xu, *ACS Catal.* **2018**, *8*, 8121-8129.

[42] L. Fan, C. Xia, F. Q. Yang, J. Wang, H. T. Wang, Y. Y. Lu, *Sci. Adv*. **2020**, *6*, eaay3111.

[43] H. Wang, Y.-K. Tzeng, Y. Ji, Y. Li, J. Li, X. Zheng, A. Yang, Y. Liu, Y. Gong, L. Cai, Y. Li, X. Zhang, W. Chen, B. Liu, H. Lu, N. A. Melosh, Z.-X. Shen, K. Chan, T. Tan, S. Chu, Y. Cui, *Nat. Nanotech.* **2020**, *15*, 131-137.

[44] S. Nitopi, E. Bertheussen, S. B. Scott, X. Liu, A. K. Engstfeld, S. Horch, B. Seger, I. E. L. Stephens, K. Chan, C. Hahn, J. K. Norskov, T. F. Jaramillo, I. Chorkendorff, *Chem. Rev*. **2019**, *119*, 7610-7672.

[45] X. Wang, A. Xu, F. Li, S. F. Hung, D. H. Nam, C. M. Gabardo, Z. Wang, Y. Xu, A. Ozden, A. S. Rasouli, A. H. Ip, D. Sinton, E. H. Sargent, *J. Am. Chem. Soc*. **2020**, *142*, 3525-3531.

[46] J. Li, Z. Wang, C. McCallum, Y. Xu, F. Li, Y. Wang, C. M. Gabardo, C.-T. Dinh, T.-T. Zhuang, L. Wang, J. Y. Howe, Y. Ren, E. H. Sargent, D. Sinton, *Nat. Catal.* **2019**, *2*, 1124-1131.

[47] Y. Huang, A. D. Handoko, P. Hirunsit and B. S. Yeo, *ACS Catal.* **2017**, *7*, 1749-1756.

[48] M. Gattrell, N. Gupta, A. Co, *J. Electroanal. Chem.* **2006**, *594*, 1-19.

[49] K. J. P. Schouten, Y. Kwon, C. J. M. van der Ham, Z. Qin, M. T. M. Koper, *Chem. Sci.* **2011**, *2*, 1902.

[50] C. M. Gunathunge, X. Li, J. Li, R. P. Hicks, V. J. Ovalle, M. M. Waegele, *J. Phys. Chem. C*. **2017**, *121*, 12337-12344.

[51] F. Li, Y. C. Li, Z. Wang, J. Li, D.-H. Nam, Y. Lum, M. Luo, X. Wang, A. Ozden, S.-F. Hung, B. Chen, Y. Wang, J. Wicks, Y. Xu, Y. Li, C. M. Gabardo, C.-T. Dinh, Y. Wang, T.-T. Zhuang, D. Sinton, E. H. Sargent, *Nat. Catal.* **2019**, *3*, 75-82.

[52] A. Eilert, F. S. Roberts, D. Friebel, A. Nilsson, *J. Phys. Chem. lett.* **2016**, *7*, 1466-1470.

[53] K. K. Patra, S. Park, H. Song, B. Kim, W. Kim, J. Oh, *ACS Appl. Energy Mater.* **2020**, *3*,

11343-11349.

[54] Y. Zhao, X. Chang, A. S. Malkani, X. Yang, L. Thompson, F. Jiao, B. Xu, *J. Am. Chem. Soc*. **2020**, *142*, 9735-9743.

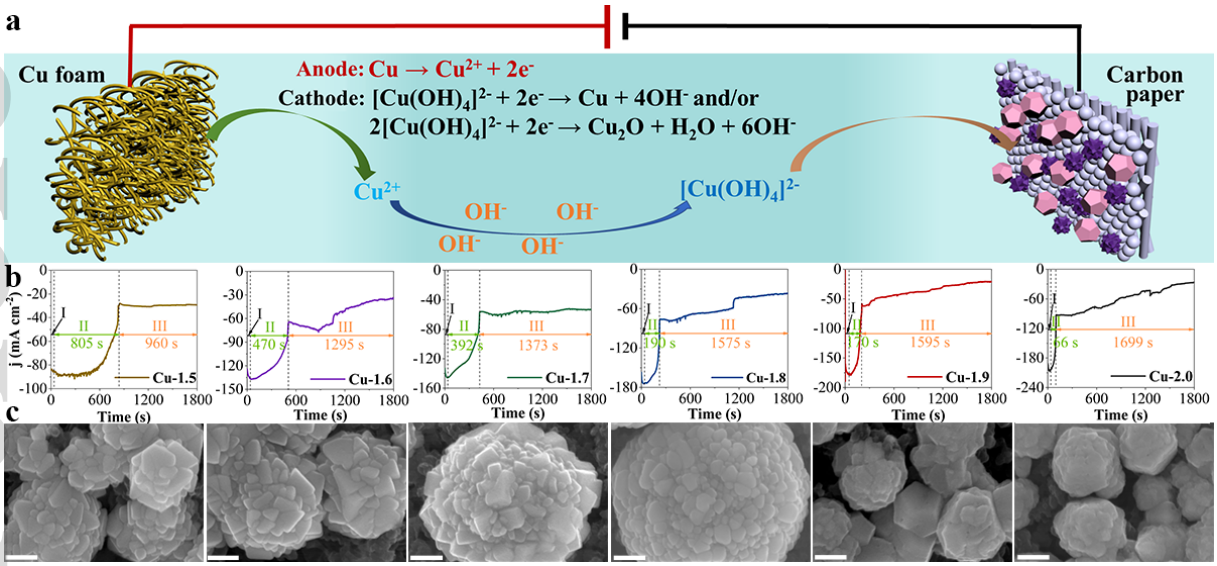

Figure 1. Electrodeposition process for the preparation of Cu catalysts. (a) Schematic of the electrodeposition process of Cu catalysts on carbon paper, (b) Time-dependent current density profiles of electrodeposition, and (c) SEM images of different Cu catalysts with varying electrodeposition voltages from 1.5 to 2.0 V (left to right). The scale bar is 200 nm.

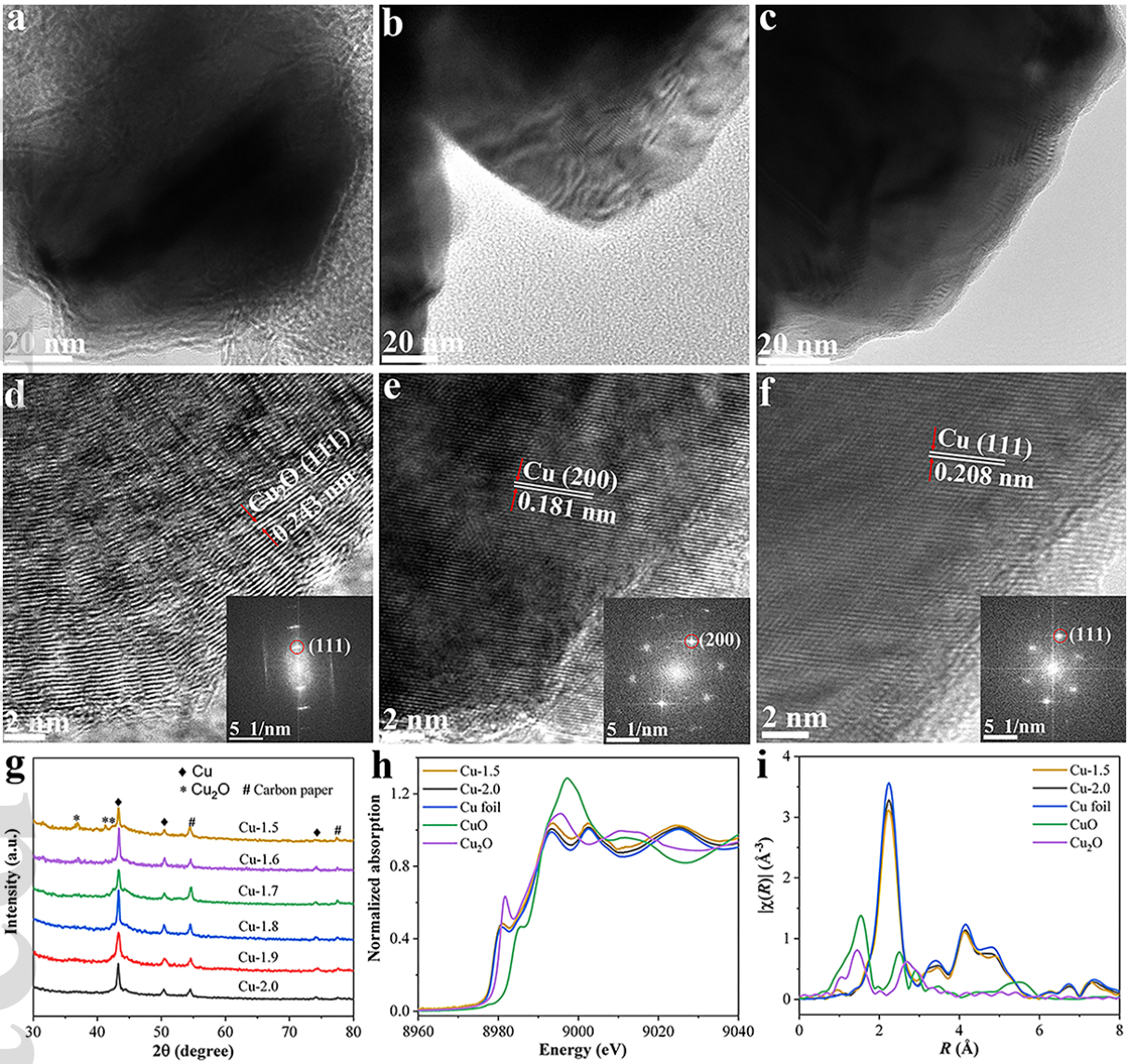

Figure 2. Structural characterization of Cu catalysts. TEM and HRTEM images of (a, d) Cu-1.5, (b, e) Cu-1.7, and (c, f) Cu-2.0. The inset shows the corresponding FFT diffraction pattern. (g) XRD patterns of different Cu catalysts. (h) Normalized Cu K-edge XANES spectra of Cu-1.5 and Cu-2.0 along with the references. (i) Corresponding K-edge EXAFS spectra.

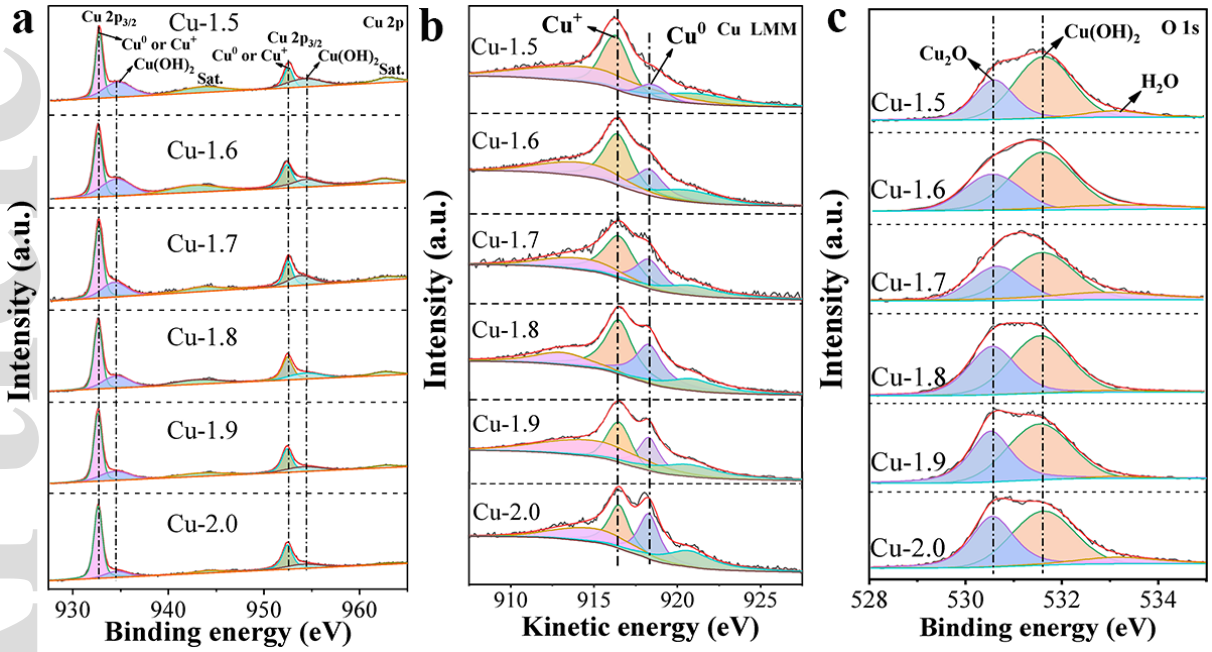

Figure 3. XPS and Auger spectra of different Cu catalysts. (a) Cu 2p, (b) Cu LMM, and (c) O 1s.

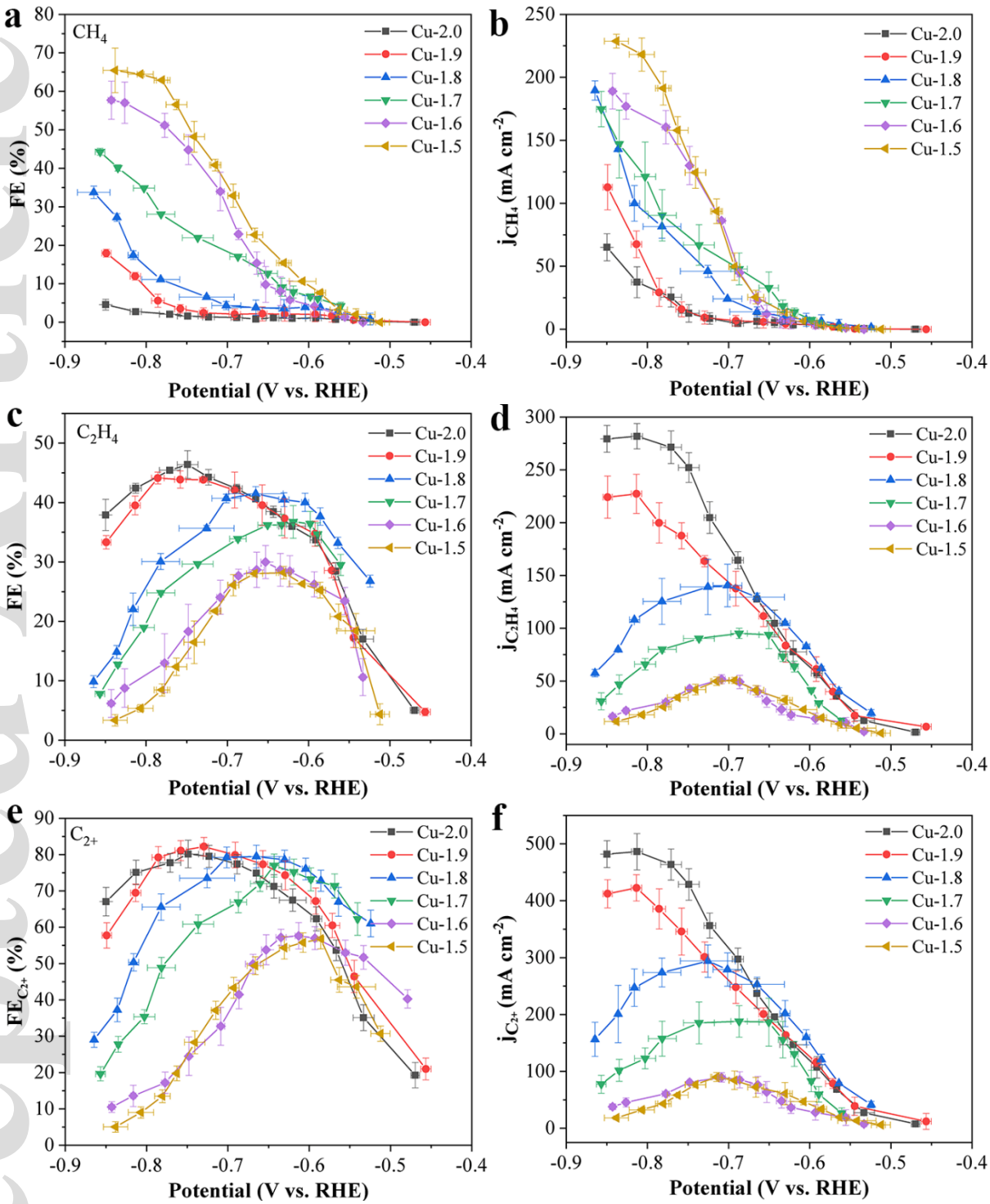

Figure 4. Performance of different Cu GDEs for CO_2 electroreduction. Faradaic efficiency and partial current densities of (a, b) CH_4, (c, d) C_2H_4, and (e, f) C_{2+} products. Error bars represent one standard deviation based on the measurements of three independent electrodes.

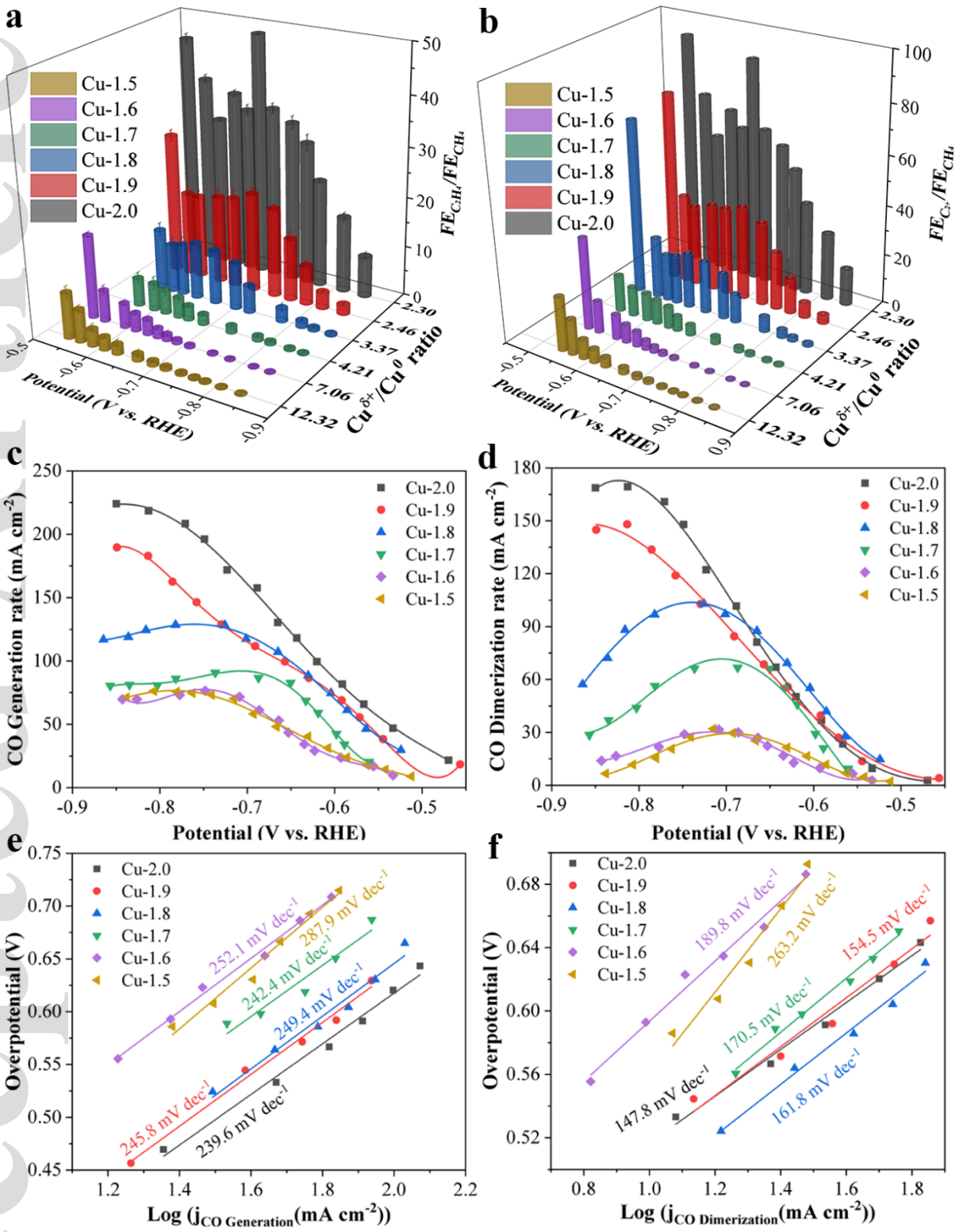

Figure 5. Origin of selectivity switch between CH_4 and C_2H_4. (a-b) The dependence of (a) $FE_{C_2H_4}/FE_{CH_4}$ and (b) FE_{C_2+}/FE_{CH_4} ratios on the $Cu^{\delta+}/Cu^0$ ratio. (c) Normalized CO generation rate. (d) Normalized CO dimerization rate. (e-f) Tafel plots of (e) CO generation and (f) CO dimerization.

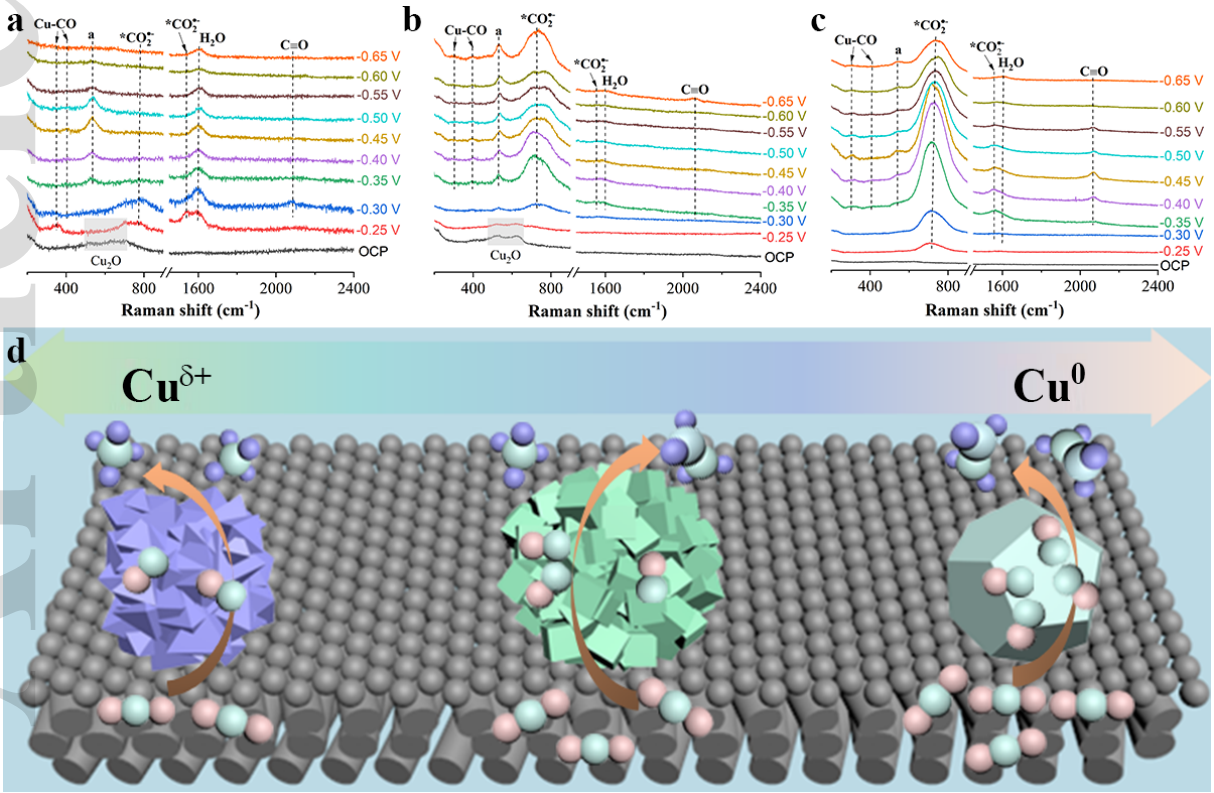

Figure 6. In-situ Raman spectra of (a) Cu-1.5, (b) Cu-1.7, and (c) Cu-2.0 GDEs at different applied potentials. (d) Schematic illustrating of selective CO_2RR towards CH_4 and C_2H_4 on different morphological Cu catalysts with tunable $Cu^{\delta+}$ contents.